ChemPhysChem

Research Article
doi.org/10.1002/cphc.202400118

Chemistry Europe
European Chemical Societies Publishing

www.chemphyschem.org

Tuning Electronic and Structural Properties of Lead-Free Metal Halide Perovskites: A Comparative Study of 2D Ruddlesden-Popper and 3D Compositions

J. F. Dalmedico,[a] D. N. Silveira,[b] L. O. de Araujo,[b] W. Wenzel,[c] C. R. C. Rêgo,*[c] A. C. Dias,[d] D. Guedes-Sobrinho,[b] and Maurício J. Piotrowski[a]

In recent decades, two-dimensional (2D) perovskites have emerged as promising semiconductors for next-generation photovoltaics, showing notable advancements in solar energy conversion. Herein, we explore the impact of alternative inorganic lattice BX-based compositions (B = Ge or Sn, X = Br or I) on the energy gap and stability. Our investigation encompasses $BA_2Ma_{n-1}B_nX_{3n+1}$ 2D Ruddlesden-Popper perovskites (for n = 1–5 layers) and 3D bulk $(MA)BX_3$ systems, employing first-principles calculations with spin-orbit coupling (SOC), DFT-1/2 quasiparticle, and D3 dispersion corrections. The study unveils how atoms with smaller ionic radii induce anisotropic internal and external distortions within the inorganic and organic lattices. Introducing the spacers in the low-layer regime reduces local distortions but widens band gaps. Our calculation protocol provides deeper insights into the physics and chemistry underlying 2D perovskite materials, paving the way for optimizing environmentally friendly alternatives that can efficiently replace with sustainable materials.

Introduction

Two-dimensional (2D) perovskites have emerged as promising next-generation photovoltaic semiconductors in recent decades,[1–5] marked by notable developments in solar energy conversion.[6–10] Despite their power conversion efficiency (PCE) slightly exceeding 16%,[11] which is lower compared to their three-dimensional (3D) counterparts (25%),[12] 2D perovskites possess intrinsic stability features.[6–10,13]

In particular, 2D metal halide perovskites (MHPs) constitute organic-inorganic layers with a vast compositional and structural phase space, leading to novel and exciting properties.[14] Among these, the [100]-oriented family stands out as the most widely utilized, comprising two essential layers. The first layer consists of n stacked MHPs, while the other incorporates organic cations as spacers along the [100] direction. This arrangement imparts higher tolerance to organic components, optimal density configuration, superior optoelectronic properties, controllability of components, and stability in the crystal structure, making it particularly well-suited for solar cells.[14,15]

The formula $A'_2A_{n-1}B_nX_{3n+1}$ denotes Ruddlesden–Popper (RP) 2D MHPs.[16–19] In this formula, A represents a monovalent organic cation, while B and X symbolize metal and halogen anions, respectively. The term A′ denotes another monovalent cation acting as an organic spacer layer, which relies on intermolecular van der Waals (vdW) weak forces.[15] The synthesis of 2D MHPs is facile at low temperatures and utilizes low-cost, abundant earth elements. Their structural and physical properties can be stoichiometrically tailored through synthesis reactions.[14]

Both 2D and 3D MHPs typically feature A = MA (methylammonium) lead iodine,[18,20,21] tin iodine,[22] or lead bromine.[23] As a result, Pb-based perovskites have emerged as affordable options for electricity production.[24] However, despite the efficiency of tin and lead-tin photovoltaic (PV) cells, their low stability[25] and risk of contamination[26] present barriers to commercialization.[27] Efforts in this direction are focused on developing ecologically friendly and low-cost technology.[28] Although lead-free compounds hold promise for efficient PV cells, they have not yet reached their full potential.[29]

The behavior of organic cations exhibits peculiar characteristics at specific temperatures in both 2D and 3D MHPs. With increasing temperature, the MA cation displays dynamic disorder within the cuboctahedral cage,[30–32] inducing more distortion and lower symmetry in the BX_6 octahedral layer.[30] In 2D MHPs, the presence of A′ = BA (butylammonium) spacers tends to alter the orientation of the inorganic lattice due to the loss of crystal symmetry, leading to a phase transition at low temperatures caused by the freezing of the orientation disorder

[a] J. F. Dalmedico, Prof. Dr. M. J. Piotrowski
Department of Physics, Federal University of Pelotas,
PO Box 354, Pelotas, RS, 96010–900, Brazil

[b] D. N. Silveira, L. O. de Araujo, Prof. Dr. D. Guedes-Sobrinho
Chemistry Department, Federal University of Paraná,
Curitiba, PR, 81531–980, Brazil

[c] Prof. Dr. W. Wenzel, Prof. Dr. C. R. C. Rêgo
Institute of Nanotechnology Hermann-von-Helmholtz-Platz,
Karlsruhe Institute of Technology,
76021 Karlsruhe, Germany
E-mail: celso.rego@kit.edu

[d] Prof. Dr. A. C. Dias
Institute of Physics and International Center of Physics,
University of Brasília,
Brasília, DF, 70919–970, Brazil

Supporting information for this article is available on the WWW under https://doi.org/10.1002/cphc.202400118

of the organic moieties.[33] Despite presenting a static behavior, these spacers strongly interact with nearby B–X octahedral bonds, ultimately reducing the rotational freedom of MA.[32] Room temperature allows one to control the crystal's or grains' local phase.[34] Limited knowledge exists regarding the underlying physics behind how lattice softness and structural dynamics impact the physical properties of 2D MHPs, especially for $n > 1$. Accurately predicting the structural dynamics of 2D MHPs using first-principles modeling is challenging.[14] Hence, we investigate the electronic and structural properties of MHPs through first-principles calculations.

We employed an automated scientific workflow developed within the SimStack framework,[35] coupled with a Density Functional Theory (DFT) protocol incorporating SOC, vdW, and DFT-1/2 quasiparticle corrections to enhance the band gap description. This study investigates 2D RP perovskites, denoted by the formula $BA_2MA_{n-1}B_nX_{3n+1}$. We explore how electronic and structural properties evolve by transitioning to environmentally friendly metal alternatives to Pb (B = Ge, Sn) and by varying the halogen component (X = I, Br). The structural configurations encompass a range of layers from $n = 1$ to 5, with the organic spacer BA separating the inorganic B_nX_{3n+1} octahedra. Additionally, as part of our standard protocol, we analyze their 3D counterparts ($MABX_3$) for comparison. The analysis of these systems establishes a characterization protocol, offering insights into how distortions, tilting, and atomic radii influence the optical properties of tunneling and the thermodynamic stability of inorganic octahedra in both core and interface regions.

Methodology

Our study generated all raw data using Workflow Active Nodes (WaNos) within the SimStack framework (SimStack's documentation).[35] Our dataset resulted from integrating four distinct WaNos, as illustrated in Figure 1, all details about the WaNos and their respective documentation are available on our GitHub repositories: Mult-It, DFT-VASP, DFT-half, and DB-Generator. Additionally, a Colab notebook was utilized to facilitate the extraction of structural and electronic properties across the MHP systems. Below, we provide a detailed overview of the parameters employed in each workflow step.

Structural Configurations

We selected 2D RP MHPs with the organic-inorganic conformation $BA_2MA_{n-1}B_nX_{3n+1}$ for study, replacing B = Pb with B = Ge, Sn, and considering X = I and Br to enhance tunability. The investigation encompasses configurations with n layers ranging from 1 to 5, featuring the organic spacer BA separating the inorganic B_nX_{3n+1} octahedra. Additionally, we explore the 3D conformation $MABX_3$ ($n = \infty$), where organic cation spacers are absent. Figure 2 illustrates representative depictions for (a) 2D and (c) 3D systems. To characterize the structural composition of hybrid perovskites, we evaluate the thickness of the organic (l_{org}) and inorganic (L) regions, with the latter further divided into the interface (l_{int}) and core (l_{core}) regions (see Figure 2(b)).

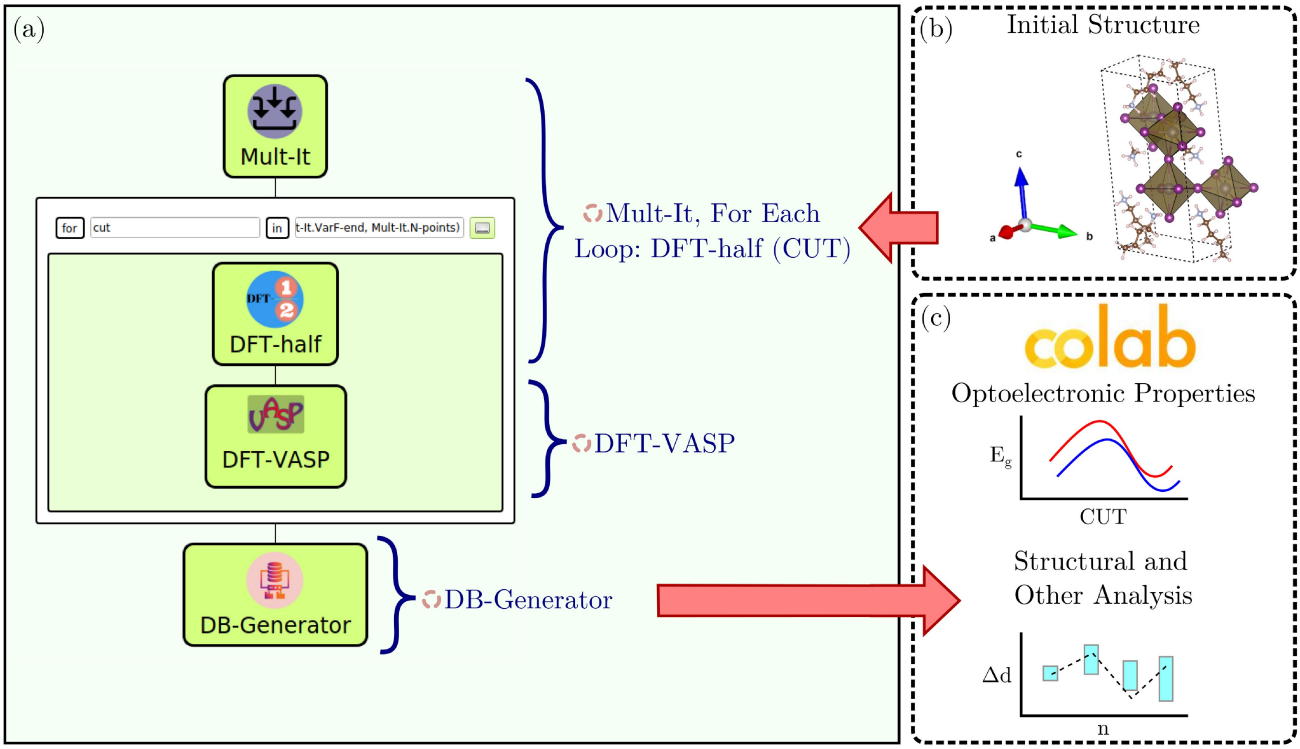

Figure 1. (a) Comprehensive SimStack workflow used for calculating the properties of two-dimensional Ruddlesden-Popper metal halide perovskites (2D RP MHPs), integrating a series of WaNos: Mult-It, DFT-half, DFT-Vasp, and DB-Generator. Mult-It: creation and management of data lists. DFT-VASP: performs Density Functional Theory calculations from the geometry configurations used as (b) input. DB-Generator: compiles the results into a database. Additionally, the workflow connects the dataset generated via workflow with a (c) Colab notebook to treat structural and electronic MHP properties. All links are provided above.

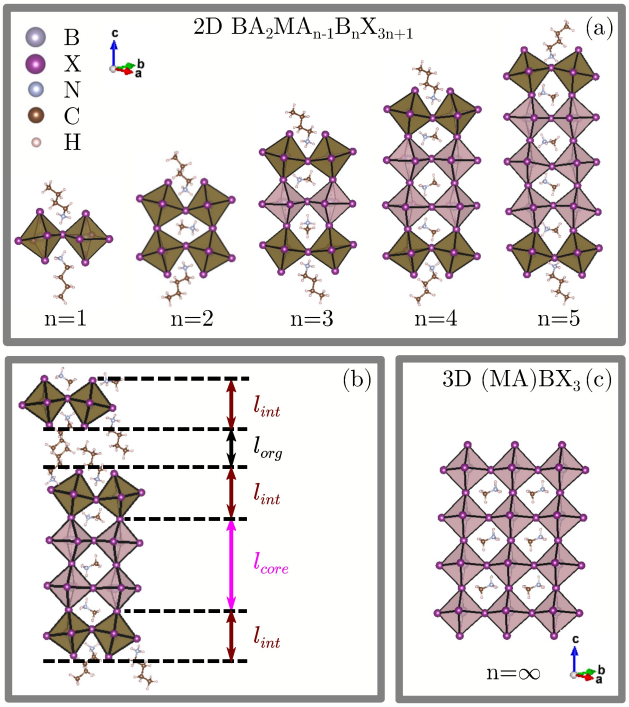

Figure 2. (a) Two-dimensional Ruddlesden-Popper Metal Halide Perovskites (2D RP MHPs) with varying numbers of layers, denoted as $n = 1$, 2, 3, 4, and 5. (b) Division of the inorganic layer thickness L into the interface l_{int} and core l_{core} regions. (c) Three-dimensional Metal Halide Perovskite (3D MHP) representation, where $n = \infty$.

Additionally, we estimate the spacer penetration degree (Δz) over the top and bottom interfaces of L. To quantify structural distortions within the inorganic lattice, we calculate the bond length distortion (Δd)[36–38] beyond the metal-halogen bonding BX. Similarly, octahedral tilting is determined from the bond angle variance (σ^2),[38] which correlates with the angles BXB and bond BX distortions. Further details are available in the Supporting Information (SI) material. It is crucial to highlight that to leverage local symmetry. We combined two unit cells into a $2 \times 1 \times 1$ tetragonal supercell for the 2D MHPs. In contrast, a cubic unit cell was employed for the 3D composites.

Total Energy Calculations

This study's geometry optimization and optoelectronic properties calculation protocol is based on DFT.[39,40] We have considered the scalar relativistic equation of states (Koelling-Harmon)[41] as well as the semilocal generalized gradient approach with the Perdew–Burke–Ernzenhof (PBE) exchange-correlation functional.[42] The Kohn–Sham (KS) equations were solved using the projector augmented wave (PAW) method,[43,44] as implemented in the Vienna *ab initio* simulation package (VASP).[45,46] As core electrons are accounted for with a fully relativistic treatment. In contrast, valence electrons are modeled using a scalar-relativistic approximation. The second variational approach included SOC effects in the valence states for the PBE functional.

Structural optimizations were conducted by minimizing the stress tensor and atomic forces until the atomic forces were below 0.01 eV/Å. A plane-wave cutoff energy of 2×ENMAX was utilized, where ENMAX represents the highest recommended cutoff energy for each element. The structural, energetic, and electronic properties were obtained using a plane-wave cutoff energy of 500 eV. Within the KS self-consistent cycle, a total energy convergence criterion of 10^{-6} eV was applied.

Total energy calculations involving Brillouin-Zone (BZ) integration in reciprocal space were performed using Monkhorst and Pack **k**-meshes of $4 \times 4 \times 3$ for tetragonal and orthorhombic 2D/quasi-2D, and $8 \times 8 \times 8$ for cubic 3D bulk unit cells. Given the significance of organic chain spacers and cations in the form of dipole moments, vdW interactions were included through the D3 correction.[47,48] Notably, analyzing weakly interacting systems, particularly where the unit cell size could impact the dynamic freedom of MA cations due to long-range interactions, poses a challenge in MHPs.[31] Further computational details, including convergence tests, are presented in the SI material (Tables S1–S9). All the aforementioned calculation parameters were defined within the Active Node DFT-VASP in our automatization via simstack.

Electronic Property Calculations

We employed the DFT-1/2 quasi-particle correction method for band gap energy calculations as a relativistic correction.[49] This method maintains computational costs at the standard DFT level and is based on Slater's transition technique,[49–51] expanded for crystalline structures. It applies a half-occupation associated with the KS potential via $V_{\text{mod,KS}}(\vec{r}) = V_{\text{KS}}(\vec{r}) - V_s(\vec{r})$. The correction maximizes the gap energy non-empirically, modifying the KS potential $V_{\text{mod,KS}}(\vec{r})$ by subtracting the self-energy potential $V_s(\vec{r})$ given by $V_s(\vec{r}) = \Theta(\vec{r}, CUT)\left[V_{ae}(\vec{r}) - V_{ae-1/2}(\vec{r})\right]$. Here, the self-energy describes the difference between the all-electron (ae) same potential $V_{ae}(\vec{r})$ and its all-electron half-occupied potential $V_{ae-1/2}(\vec{r})$, considering a cutoff radius function $\Theta(\vec{r}, CUT)$ determined variationally to prevent Coulomb tails' overlap into neighboring atom sites (complementary details in the SI). In our Simstack workflow for DFT-half calculations, the cutoff radius is individually optimized for each 3D system. Leveraging the consistent chemical environment of atoms within specific families of compounds, this optimized cutoff radius is then utilized for maximizing the band gap in the 2D MHPs. This approach is supported by its exceptional transferability performance, as in various studies.[52–54]

The idea is to include an ionization term in the valence band maximum (VBM) and conduction band minimum (CBM), which are not accounted for in the KS gap energy calculations, achieving exceptional accuracy compared to experimental data.[18,52,54,55] The band gap energy analysis followed a sequence of protocols starting from the standard PBE exchange-correlation functional and incorporating corrections such as D3, SOC, and DFT-1/2. We employed a Workflow Active Node (WaNo) DFT-VASP[35,56,57] in the Simstack workflow to simplify the protocol complexity of this high volume of implemented calculations. These simplified protocols allow for better monitoring of different structural configurations with multiple layers and are less time-consuming.

Results and Discussion

Structural Analysis

Initially, we provide a detailed description of the structural information (i.e., the organic and inorganic layers) of the Ge- and Sn-based 2D and 3D MHPs and their halogen combinations. We found that the calculated lattice parameters for 2D and 3D MHPs are in good agreement with both experimental and theoretical reports (refer to Table S10), displaying a deviation of

less than 10% when compared to literature data. Consequently, the stability and optoelectronic properties calculated are based on correct structural configurations. Given the absence of temperature effects, our lattice parameters and angles suggest triclinic-like behavior. Figure 3 compiles structural properties as a function of the layer number (n) for four BX combinations (GeBr, GeI, SnBr, and SnI). The parameters include L for the thickness of the inorganic layer with its subdivisions (l_{int} for interface octahedra, l_{core} for core octahedra), l_{org} for the organic layer, as well as Δz, Δd, σ^2, and θ_{BXB}.

Observing Figure 3(a), L values exhibit a linear correlation with n for all BX compositions, aligning with the trends in panels (b) and (c), i.e., $L = l_{int}$ ($n = 1$), $L = 2l_{int}$ ($n = 2$), and $L = 2l_{int} + l_{core}$ ($n = 3$–5). This result aligns with prior work on 2D PbI-based MHPs,[54] demonstrating a more subtle manifestation of l_{int}. This difference does not indicate a negligible effect of local octahedral distortions from interface stress between inorganic and organic layers, but rather underscores a significant adaptability facilitated by the smaller atomic size of B atoms (Ge and Sn) compared to Pb.

Aiming for a deeper understanding of the organic spacers regions, Figure 3(d) reveals a corresponding range of values for l_{org}, except for $n = 1$, within the interval region corresponding to the triclinic phase.[58] Also, as per the numerical description in Table S11, L increases linearly, primarily driven by contributions from the core region (l_{core}), with minor fluctuations around an average value for the interface region (l_{int}). In contrast, l_{org} peaks at $n = 1$ across all systems, exhibiting a larger value as lower ionic radii atoms accommodate B and X in the inorganic lattice (GeBr > GeI > SnBr > SnI). For $n > 1$, l_{org} decreases around an average value. This behavior could be linked to the absence of MA, introduced over $n \geq 2$, and the strong dipole moment between BA spacers from different organic layers, which decreases with additional layer stacking.

We analyzed the details of the BA spacer interaction with the inorganic layer part, as depicted in Figure 3(e,f), since differences concerning the metal size (i.e., Ge and Sn) may exhibit different structural behavior when compared with quasi-2D lead-based MHPs.[54] Thus, we calculated the penetration degree (Δz) of the BA spacer in the octahedra over the top and bottom interfaces (see panel (k)). Δz exhibits a global increase with the growth of the B and X ionic radii. This trend is inversely proportional to l_{org} and could signify a stronger dipole effect of the BA spacer,[31] especially in Ge-based compositions. However, Δz increases on average until $n = 3$ and then decreases for more stacking in all systems, indicating more stress and compression in L for SnX-based compositions. The results suggest that 2D MHPs for $n = 3$ represent an equilibrium phase

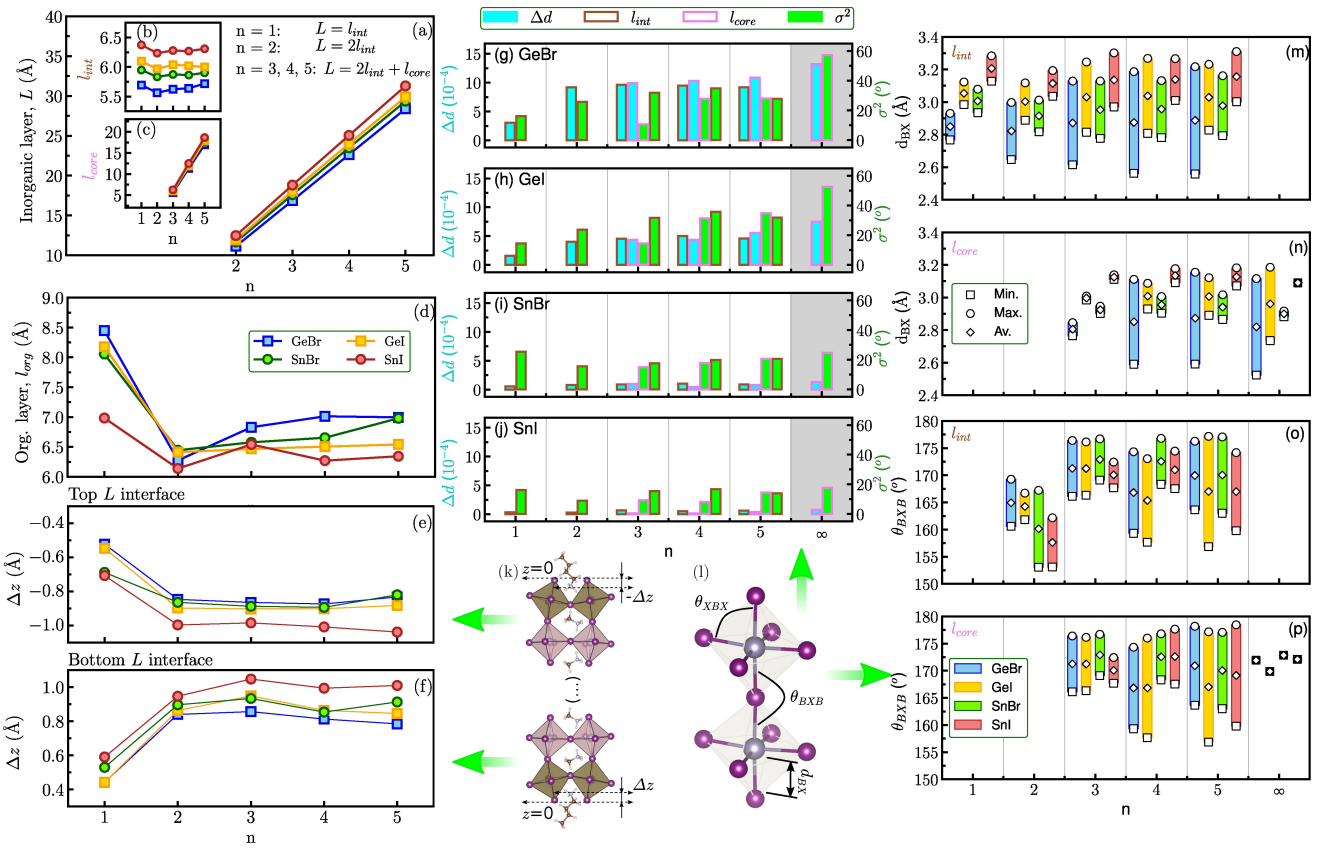

Figure 3. The structural analysis of all BX-based systems yielded the following results: (a) thickness data (L) for the inorganic lattice, along with its subdivisions, (b) thickness of the interface region (l_{int}), (c) thickness of the core region (l_{core}), (d) thickness of the organic lattice (l_{org}), (e) spacer penetration degree (Δz) over the top interface of L, (f) Δz over the bottom interface of L, both explained in the scheme denoted by (k). For internal distortions, the Δd and σ^2 results describe the 2D and 3D compounds for: (g) GeBr, (h) GeI, (i) SnBr, and (j) SnI, within both l_{int} and l_{core}. (l) The scheme represents the base variables, such as (m–n) the B–X bond length (d_{BX}) for the discussed internal distortions, and (o–p) the octahedral tilting angle (θ_{BXB}), also inside l_{int} and l_{core}.

where MA surpasses the spacer in number and rigidness of the inorganic lattice. Numerical values for the cation BA penetration factor in 2D compositions can be found in Table S12. This analysis quantifies the penetration of the organic cation at both the lower and upper borders, delineating the separation between the organic and inorganic lattices.

As octahedral distortions can directly affect the optical and electronic properties of 2D and 3D MHPs, we conducted a thorough analysis for all BX compositions, considering regional distortions through the bond length distortion Δd, as shown in Figure 3(g–j). In general, adding the BA spacer in 2D systems reduced all distortions compared to bulk compositions. Δd exhibited increasing distortion within the BX_6 lattice with added stacking layers across all compositions. Among compositions with the same layer stacking in different systems, Δd converged to zero while shifting the B metal and X halogen to heavier elements. This change (B = Ge→Sn and then X = Br→I) resulted in a centrosymmetric behavior and less distortion.

Within the inorganic lattice, l_{core} tends to exhibit higher distortion ($\Delta d(l_{core}) > \Delta d(l_{int})$), particularly in GeBr-based MHPs due to the noncentrosymmetric behavior of Ge and its smaller ionic radius.[59,60] Conversely, SnI-based MHPs behave more centrosymmetrically, resulting in lower distortion in l_{core} ($\Delta d(l_{core}) < \Delta d(l_{int})$). The intermediate systems, GeI- and SnBr-based, along with their layered conformations, maintain both centro- and noncentrosymmetric behavior due to the presence of Ge and Sn metals, making them exceptions by not having l_{core} dominant in all compositions.

When comparing l_{core} with l_{int} for $n \geq 3$, the distortion in GeBr-based compositions tends to be less than 20% ($\Delta d(l_{core}) < \Delta d(l_{int})$), whereas it is almost 2× lower in SnI-based compositions ($\Delta d(l_{core}) > \Delta d(l_{int})$). For compositions with l_{int} only ($n = 1$, 2), the inorganic lattice experiences an increase in distortion from $n = 1$ to 2, ranging from a maximum of 3× (GeBr), 2.5× (GeI), 1.3× (SnBr), down to zero (SnI-based), highlighting the effects of adding MA cations. In Table S13, a comparative analysis of Δd values by octahedron (O_j) is provided for all 2D and 3D compositions in both interface (l_{int}) and core (l_{core}) regions.

Additionally, distortions within the octahedron were quantified using the bond angle variance, σ^2. As depicted in Figure 3(g–j), a trend similar to Δd is observed for σ^2. The 2D compositions exhibited σ^2 values up to 2× lower compared to their analogous 3D structures, accompanied by a reduction in values attributed to the alteration of B and X atoms. Notably, l_{core} displayed lower values ($\sigma^2(l_{core}) < \sigma^2(l_{int})$) for $n = 3$, 4 within L, with the exception of $n = 5$ in Ge-based systems ($\sigma^2(l_{core}) > \sigma^2(l_{int})$) and Sn-based systems ($\sigma^2(l_{core}) \approx \sigma^2(l_{int})$). These findings suggest that σ^2 is significantly influenced by the spacer's dipole moment, experiencing a reduction from $n = 5$, where more MA is present than BA. During the transition from $n = 1 \rightarrow 2$, σ^2 almost doubled in all systems when transitioning to a heavier BX pair, except for the SnBr-based system, which exhibited a distortion reduction by half. This system demonstrated the highest σ^2 among all monolayered systems ($n = 1$), indicating potential stress in l_{int} induced by the spacer. A comprehensive analysis of σ^2 values by O_j is provided in Table S14.

To further elucidate the distortions highlighted by Δd, we examine in Figure 3(m, n) the minimum, maximum, and average values for the bond lengths d_{BX} (depicted in panel (l)) calculated for the interface (l_{int}) and core (l_{core}) regions. From the d_{BX} values, we observe greater variations in metal-halogen bonds for atoms with smaller ionic radii, leading to corresponding variations in Δd. Generally, d_{BX} tends to increase with more stacking layers in both l_{int} and l_{core} (for $n \geq 3$). The GeX-based systems exhibit more deviation from minimum to maximum values, whereas SnX-based systems are more centrosymmetric. This analysis also elucidates the effect of the BA spacer in reducing rigidity in the l_{int} region, consequently increasing stress within l_{core} due to an augmentation in layers.[31] Additionally, Table S15 provides the d_{BX} values (maximum and minimum) for equatorial and apical directions, with the apical d_{BX} values being smaller for Br-based systems in both l_{core} and l_{int}, while GeBr-based systems have the smallest bond lengths, followed by SnBr, GeI, and SnI.

Similar to Δd and d_{BX}, to clarify the distortions within the octahedron, as indicated by σ^2, we have examined in Figure 3(o, p) the minimum, maximum, and average values for the angle θ_{BXB} (illustrated in panel (l)), also calculated for l_{int} and l_{core}. Meanwhile, Table S16 segregates the bond angles θ_{BXB} between equatorial and apical directions. For $n = 1$, we observe the most distorted interval of octahedral tilting angle θ_{BXB} in their monolayer equatorial plane, with Ge-based compounds tending around 150°. For $n > 1$ structures at l_{core} and l_{int}, θ_{BXB} values tend toward 180° in the equatorial plane and apical direction. Compared with the bulk ($n = \infty$), for 2D MHPs, the θ_{BXB} tends to increase with more layers. For all compositions, the equatorial plane values experience a reduction when changing B and X atoms in the sequence GeBr > GeI > SnBr > SnI. For the apical direction, θ_{BXB} shows a tendency to open as more inorganic layers are stacked compared to bulk values, with average deviations around −4.6% in the minimum and −2.7% in maximum bond angles. These results depict a stress effect in the apical direction, compensated by the equatorial plane as a distortion function of weak forces and atomic sizes of B and X. The BX_6 octahedra tends to reduce the cuboctahedral cage volume through tilting and/or rotation due to a small cation MA, which reduces the symmetry of inorganic lattices and affects the electronic properties of the system.

Stability Analysis

We initially investigated the thermodynamic stability of both 2D and 3D configurations through the calculation of formation enthalpies (ΔH_f), as illustrated in Figure 4(a). Our study relied on a series of synthesis routes commonly employed in the fabrication of 2D MHPs, as reported in the literature.[33,61] These routes involve distinct chemical reactions tailored for 2D compositions, wherein the number of layers is controlled. The synthesis routes can be represented by the following reaction for 2D compositions, where n ranges from 1 to 5:

$$nH_3PO_2 + (2n+2)HX + (n-1)CH_3NH_3X + nBO_2 + 2CH_3(CH_2)_3NH_2 \rightarrow (CH_3(CH_2)_3NH_3)_2B_nX_{3n+1} + nH_3PO_3 + nH_2O. \quad (1)$$

For 3D compositions with an infinite number of layers ($n = \infty$), the synthesis follows a simpler reaction:

$$H_3PO_2 + 2HX + CH_3NH_3X + BO_2 \rightarrow (CH_3NH_3)BX_3 + H_3PO_3 + H_2O \quad (2)$$

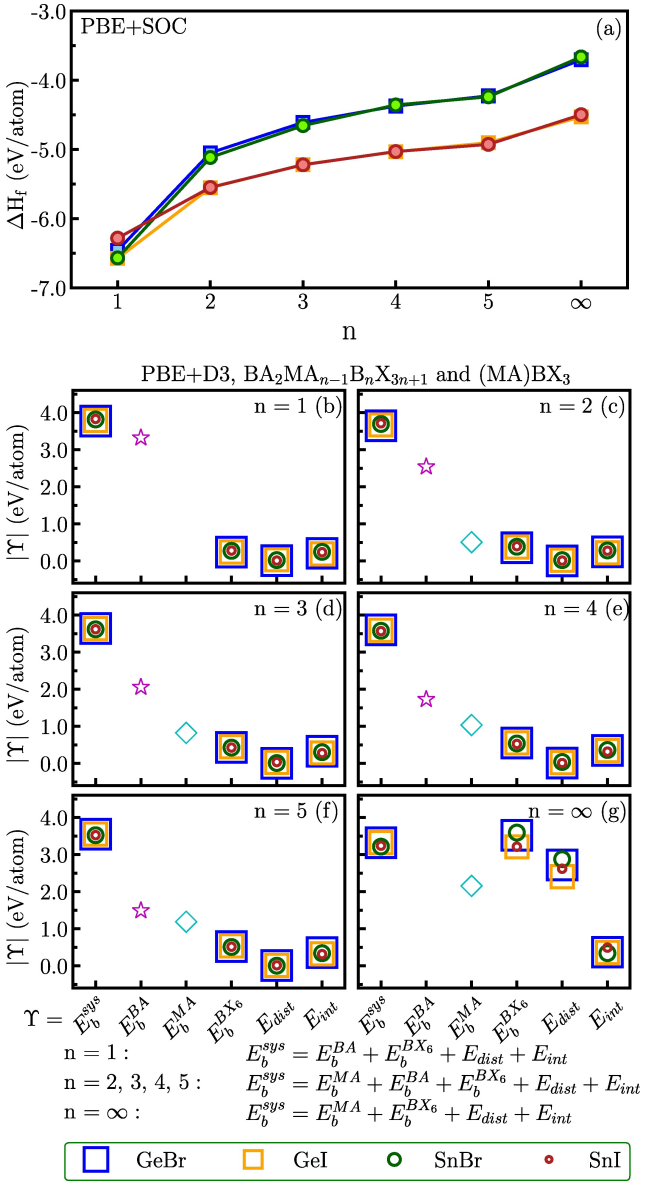

Figure 4. The stability analysis for both 2D and 3D BX-based compositions is initiated with (a) formation enthalpy (ΔH_f) at the PBE + D3 level as a function of the number of layers (n). Additionally, E_b^{sys} represents the absolute binding energy of the systems, broken down into its components: E_b^{BA} for the BA spacers, E_b^{MA} for the MA cations, $E_b^{BX_6}$ for the BX_6 octahedra, and the interaction (E_{int}) and distortion (E_{dist}) energies for varying layer numbers (n) as follows: (b) 1, (c) 2, (e) 3, (f) 4, (g) 5, and (h) ∞.

Our ΔH_f results revealed an increasing trend with the number of layers for all BX compositions, indicating that thermodynamic stability rises with a reduction in stacking layers. Importantly, the choice of halide element (X) on significantly influenced stability, with compositions generally exhibiting greater stability when X is I compared to Br. This trend was consistent across most layer numbers ($n > 1$), except for $n = 1$, where GeI- and SnBr-based systems showed the highest stability. These findings align with existing literature,[59,62] underscoring the combined influence of n and the halide element on the formation energy and stability of the system.

To enhance comprehension of energetic stability, we computed the binding energy (E_b^{sys}) for all systems. This binding energy was decomposed into individual components, including the binding energies of BA, MA, and BX_6, along with interaction (E_{int}) and distortion (E_{dist}) energies.[63,64] Figures 4(b–g) illustrate the absolute values of binding energies calculated for 2D (n = 1–5) and 3D ($n = \infty$) systems, with corresponding equations for E_b^{sys} provided in the figure. Additional details are available in the SI. A key observation is that the modulus of E_b^{sys} follows the same trend of decreasing ΔH_f magnitude with the increase in n, reaffirming the stability of 2D systems relative to 3D ones. Furthermore, there is a tendency towards increased stability due to the change in composition in B and X towards larger atomic radii.

The decomposition of the binding energy highlights the well-established behavior for 2D systems. E_b^{BA} and E_b^{MA} maintain equal values for different compositions within the same n. E_b^{BA} represents the most significant contribution among all energetic terms, affirming the cation spacer as the primary agent contributing to thermodynamic stability in all 2D configurations. Essentially, the magnitude of E_b^{BA} decreases (increases) with increasing n, while E_b^{MA} follows the opposite trend. In the sequence of energetic contributions, the values of the inorganic part of the system ($E_b^{BX_6}$) contribute slightly more than E_{int}. In contrast, in most cases, the term E_{dist} represents the energetic penalty paid due to the interaction between the organic and inorganic parts.

In the case of 3D systems, we observe a different energetic behavior, where the absence of the organic part of the spacer cations means that the greatest energetic contribution to stabilizing the system comes from the $E_b^{BX_6}$ octahedra. While the interaction energy between the MA molecules and the inorganic part is not too high, as expected, the distortion resulting from the interaction causes the magnitude of the energy penalty E_{dist} to be slightly greater than the magnitude of E_b^{MA} itself.

Electronic Analysis

We employed the DFT-1/2 quasiparticle correction protocol to accurately calculate the band gap (E_g) for all 2D RP and 3D bulk MHPs. As reported by several studies,[52–54] the DFT-1/2 method presents excellent transferability across structurally different systems with the same chemical composition. It is therefore

crucial that both 2D and 3D structures based on the same chemical composition for the inorganic part exhibit similar behavior regarding the orbital participation at the band edge. Specifically, we focused on the p-orbital from halogens, which predominantly contributes to the formation of the VBM. We perform the cutoff optimization for the MHPs by correcting the electron occupation of the p halogen orbitals at the VBM. In addition, we investigated the impact of the SOC energy portion on the band gap, as depicted in Figure 5, which demonstrates that it affects only the magnitude of the E_g but not the cutoff radius value. This is because the SOC energy (E_{SOC}) contribution from each chemical species in the MHP is relatively small, with values of $E_{SOC} = -0.010$, -0.142, -0.068, and -0.333 eV/atom for Ge, Sn, Br, and I, respectively. Thus, we used the cutoff values that maximize the band gap of the 3D structures to calculate the E_g for the 2D systems (based on the number of layers).

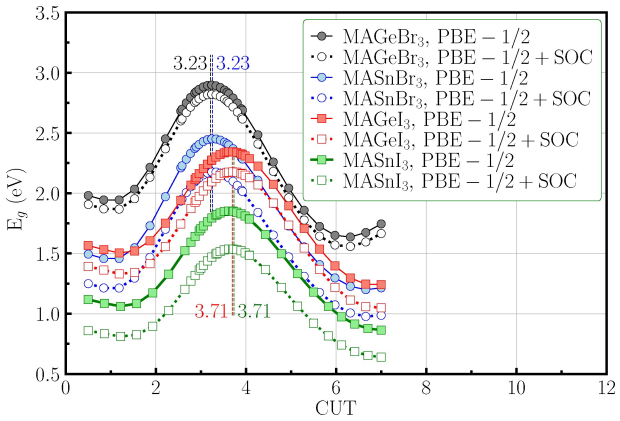

Figure 5. We apply the quasi-particle correction DFT-1/2 into two protocols to compare the impact of the SOC correction on the gap energy in 3D ($MASn_2Br_3$) compositions while optimizing the *CUT* parameter.

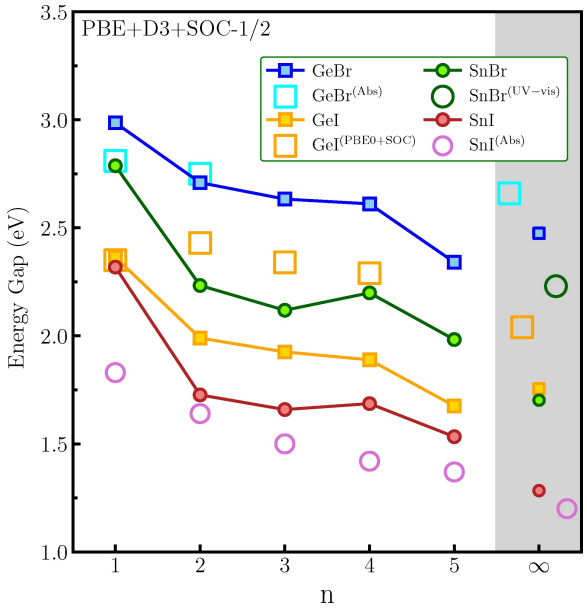

Figure 6. The electronic analysis for both 2D and 3D BX-based compositions is presented by the energy gap (E_g), using the PBE + D3 + SOC-1/2 protocol, as a function of the number of layers (n). A comparison with literature data, including optical absorbance (Abs) for GeBr,[59] UV-vis for GeI,[62] PBE0 + SOC protocol for SnBr,[66] and Abs for SnI[65] is provided.

We calculated the E_g for all 2D RP and 3D bulk MHPs, considering the B (Ge or Sn) and X (Br or I) combinations as a function of the number of layers, using the PBE + D3 + SOC-1/2 protocol, as shown in Figure 6. Our results show a narrowing of the energy gap primarily driven by the increasing n for all 2D compositions, which is consistent with previous findings in optical absorbance (Abs) studies.[59,65] Interestingly, we observed differences in the Abs protocol for systems, with percentage differences of −7.1% (GeBr), −7.9% (GeI), −20.9% (SnBr), and −1.5% (SnI).

Thus, systems characterized first by larger ionic radii halogens (I) and, then, by larger metal (Sn), showed narrower energy gaps. For the $n = 1 \rightarrow 2$ transition there occurs a steep descent, with crescent deviations of approximately −10%, −20%, −25%, and −35% for GeBr, GeI, SnBr, and SnI, respectively. This result can be attributed to the addition of MA cations within the cuboctahedral cage of the inorganic lattice ($n = 2$). In sequence, the trend of E_g decreases by adding more layers and converges to D bulk values in two distinct trends. For 2D Ge-based MHPs, a drop is observed at $n = 5$, resulting in a lower energy gap compared to 3D ($E_g(n = 5) < E_g(n = \infty)$). Conversely, for 2D Sn-based, we found a peak at $n = 4$. These anomalies could be attributed to the metal's centro- and noncentrosymmetric behavior.

Changing the composition greatly affected the structural properties, directly tuning the stability and electronic properties for both 2D and 3D compositions. The addition of the BA spacer led to a natural supercell increase in c_0, a peak in l_{org} thickness in $n = 1$ compositions, and a reduction in distortion. This addition also caused an increase in octahedral tilting and enhanced energetic stability, notably widening the gap between CBM and VBM for $n = 1$, 2. The phenomenon of a narrower energy gap in Ge-based compositions at $n = 5$ compared to 3D arises from a shift in internal octahedral distortion σ^2 from l_{int} to l_{core}. For the Sn-based anomaly at $n = 4$, an energy gap opening could be attributed to reduced tilting θ_{BXB}. Subsequent reductions in E_g stem from stacking additional layers, as described in the literature,[67] coupled with increased internal and external distortion across the inorganic lattice due to the incremental addition of MA cations. Furthermore, wider band gaps were observed with smaller ionic radii for both B and X. Despite the high distortions in GeX-based systems, SnBr compositions exhibited the second most pronounced energy gap opening, albeit with significantly fewer distortions, owing to the contribution of Br in the VBM.

Conclusions

In our study, we investigated how alternative inorganic lattice compositions (BX) influence the energy gap and stability of Ge- and Sn-based metal halide perovskites (MHPs) with X = Br and I. Employing first-principle calculations integrating SOC, DFT-1/2 quasiparticle, and D3 dispersion corrections, we thoroughly

analyzed both 2D Ruddlesden-Popper (RP) perovskites ($BA_2MA_{n-1}B_nX_{3n+1}$, with $n = 1$–5 layers) and 3D bulk systems ($(MA)BX_3$). Our investigation sheds light on the implications of novel BX combinations for predicting properties essential for optoelectronic applications.

Our findings provide a deep understanding of the structural properties and distortions in both 2D and 3D MHPs based on Ge and Sn. The calculated lattice parameters align well with experimental and theoretical data, validating the stability and optoelectronic properties derived from accurate structural configurations. Structural analyses revealed linear correlations between core layer thickness and layer number (n) across various BX combinations, highlighting the adaptability of MHPs to different atomic sizes. Additionally, the presence of MA cations influenced the rigidity of the inorganic lattice, leading to variations in layer thickness and penetration degree. Distortions within the octahedral lattice, influenced by composition and stacking layers, affected optical and electronic properties, with generally lower distortions observed in 2D compared to 3D compositions. Notably, Ge- and Sn-based systems exhibited distinct behaviors owing to atomic properties.

Examining thermodynamic stability and energetic contributions, our analysis via formation enthalpies revealed increasing stability with decreasing stacking layers, emphasizing the significant role of BA cations in stabilizing 2D configurations (with generally I-based compositions being more stable than Br-based ones). The decomposition of binding energy underscored the dominance of BA in stabilizing 2D systems and highlighted the energetic contributions of the inorganic lattice. For electronic properties, the DFT-1/2 correction protocol with SOC elucidated the band gap trends, primarily decreasing with increasing n in 2D compositions. Anomalies in band gap behavior were attributed to specific compositions and layer numbers, reflecting structural nuances. For instance, the band gap variations were influenced by the ionic radii of both the metal (B) and halogen (X). Generally, wider band gaps were observed for compositions with smaller ionic radii. However, anomalies were noted, such as wider band gaps for SnBr compositions despite higher distortions and narrower band gaps for GeX systems, particularly in the case of $n = 5$.

Overall, our study underscores the importance of considering composition, layer number, and structural properties in analyzing the energetic and electronic characteristics of MHPs. These insights advance our understanding of their potential applications in optoelectronics and provide a framework for optimizing their properties. By elucidating the underlying physics and chemistry of 2D perovskite materials, this research paves the way for the development of environmentally friendly alternatives with enhanced performance and sustainability.

An important perspective lies in further exploring the excitonic and optical properties of these systems, as they can significantly impact the band gap properties, including absorption spectrum, optical properties, and exciton binding energy, particularly in 2D MHPs. The reduced dimensionality and confinement of charge carriers in these systems can enhance exciton effects, potentially leading to stronger electron-hole interactions.

Acknowledgements

Authors thank the Rio Grande do Sul Research Foundation – FAPERGS, the Federal District Research Support Foundation FAPDF, (grants 00193-00001817/2023-43 and 00193-00002073/2023-84), the National Council for Scientific and Technological Development – CNPq (M.J.P. grant number 307345/2021-1 and A.C.D. grant number 408144/2022-0), and the Coordination for Improvement of Higher Level Education – CAPES (finance Code 001) for the financial support. W.W. acknowledge the financial support by Deutsche Forschungsgemeinschaft (DFG, German Research Foundation) through project WE 1863/29-1. W.W. and C.R.C.R. thank the German Federal Ministry of Education and Research (BMBF) for financial support of the project Innovation-Platform MaterialDigital (www.materialdigital.de) through project funding FKZ number 13XP5094A. Authors thank also the computational infrastructure provided to the Karlsruhe Institute of Technology (KIT) and the Department of Physics from the Federal University of Pelotas. This work also used resources of the "Centro Nacional de Processamento de Alto Desempenho em São Paulo (CENAPAD-SP)", CIMATEC SENAI at Salvador – BA, Brazil for the partnership, support through the Ogun Supercomputer, "Laboratório Central de Processamento de Alto Desempenho" (LCPAD) financed by FINEP through CT-INFRA/UFPR projects, and of the "Centro Nacional de Supercomputação (CESUP-UFRGS)", which we thank. We acknowledge support by the KITPublication Fund of the Karlsruhe Institute of Technology. Open Access funding enabled and organized by Projekt DEAL.

Conflict of Interests

The authors declare no conflict of interest.

Data Availability Statement

The data that support the findings of this study are openly available in DFT-VASP at https://github.com/KIT-Workflows/DFT-VASP, reference number 3.

Keywords: metal halide perovskites · density functional theory · structural, stability · electronic properties

[1] J.-C. Blancon, A. V. Stier, H. Tsai, W. Nie, C. C. Stoumpos, B. Traoré, L. Pedesseau, M. Kepenekian, F. Katsutani, G. T. Noe, J. Kono, S. Tretiak, S. A. Crooker, C. Katan, M. G. Kanatzidis, J. J. Crochet, J. Even, A. D. Mohite, *Nat. Commun.* **2018**, *9*.
[2] G. Wu, X. Li, J. Zhou, J. Zhang, X. Zhang, X. Leng, P. Wang, M. Chen, D. Zhang, K. Zhao, S. F. Liu, H. Zhou, Y. Zhang, *Adv. Mater.* **2019**, *31*.
[3] Y. Liu, S. Akin, L. Pan, R. Uchida, N. Arora, J. V. Milić, A. Hinderhofer, F. Schreiber, A. R. Uhl, S. M. Zakeeruddin, A. Hagfeldt, M. I. Dar, M. Grätzel, *Sci. Adv.* **2019**, *5*.

[4] B.-E. Cohen, Y. Li, Q. Meng, L. Etgar, *Nano Lett.* **2019**, *19*, 2588–2597.
[5] A. S. R. Bati, M. Batmunkh, J. G. Shapter, *Adv. Energy Mater.* **2019**, *10*.
[6] H.-S. Kim, C.-R. Lee, J.-H. Im, K.-B. Lee, T. Moehl, A. Marchioro, S.-J. Moon, R. Humphry-Baker, J.-H. Yum, J. E. Moser, M. Grätzel, N.-G. Park, *Sci. Rep.* **2012**, *2*.
[7] H. Zhou, Q. Chen, G. Li, S. Luo, T.-b. Song, H.-S. Duan, Z. Hong, J. You, Y. Liu, Y. Yang, *Science* **2014**, *345*, 542–546.
[8] M. M. Tavakoli, P. Yadav, R. Tavakoli, J. Kong, *Adv. Energy Mater.* **2018**, *8*.
[9] X. Zheng, Y. Hou, C. Bao, J. Yin, F. Yuan, Z. Huang, K. Song, J. Liu, J. Troughton, N. Gasparini, C. Zhou, Y. Lin, D.-J. Xue, B. Chen, A. K. Johnston, N. Wei, M. N. Hedhili, M. Wei, A. Y. Alsalloum, P. Maity, B. Turedi, C. Yang, D. Baran, T. D. Anthopoulos, Y. Han, Z.-H. Lu, O. F. Mohammed, F. Gao, E. H. Sargent, O. M. Bakr, *Nat. Energy* **2020**, *5*, 131–140.
[10] M. Kim, J. Jeong, H. Lu, T. K. Lee, F. T. Eickemeyer, Y. Liu, I. W. Choi, S. J. Choi, Y. Jo, H.-B. Kim, S.-I. Mo, Y.-K. Kim, H. Lee, N. G. An, S. Cho, W. R. Tress, S. M. Zakeeruddin, A. Hagfeldt, J. Y. Kim, M. Grätzel, D. S. Kim, *Science* **2022**, *375*, 302–306.
[11] C. Liang, H. Gu, Y. Xia, Z. Wang, X. Liu, J. Xia, S. Zuo, Y. Hu, X. Gao, W. Hui, L. Chao, T. Niu, M. Fang, H. Lu, H. Dong, H. Yu, S. Chen, X. Ran, L. Song, B. Li, J. Zhang, Y. Peng, G. Shao, J. Wang, Y. Chen, G. Xing, W. Huang, *Nat. Energy* **2020**, *6*, 38–45.
[12] J. Jeong, M. Kim, J. Seo, H. Lu, P. Ahlawat, A. Mishra, Y. Yang, M. A. Hope, F. T. Eickemeyer, M. Kim, Y. J. Yoon, I. W. Choi, B. P. Darwich, S. J. Choi, Y. Jo, J. H. Lee, B. Walker, S. M. Zakeeruddin, L. Emsley, U. Rothlisberger, A. Hagfeldt, D. S. Kim, M. Grätzel, J. Y. Kim, *Nature* **2021**, *592*, 381–385.
[13] L. N. Quan, M. Yuan, R. Comin, O. Voznyy, E. M. Beauregard, S. Hoogland, A. Buin, A. R. Kirmani, K. Zhao, A. Amassian, D. H. Kim, E. H. Sargent, *J. Am. Chem. Soc.* **2016**, *138*, 2649–2655.
[14] J.-C. Blancon, J. Even, C. C. Stoumpos, M. G. Kanatzidis, A. D. Mohite, *Nat. Nanotechnol.* **2020**, *15*, 969–985.
[15] L. Mao, C. C. Stoumpos, M. G. Kanatzidis, *J. Am. Chem. Soc.* **2018**, *141*, 1171–1190.
[16] S. N. Ruddlesden, P. Popper, *Acta Crystallogr.* **1957**, *10*, 538–539.
[17] S. N. Ruddlesden, P. Popper, *Acta Crystallogr.* **1958**, *11*, 54–55.
[18] C. C. Stoumpos, D. H. Cao, D. J. Clark, J. Young, J. M. Rondinelli, J. I. Jang, J. T. Hupp, M. G. Kanatzidis, *Chem. Mater.* **2016**, *28*, 2852–2867.
[19] Z. Qin, S. Dai, C. C. Gajjela, C. Wang, V. G. Hadjiev, G. Yang, J. Li, X. Zhong, Z. Tang, Y. Yao, A. M. Guloy, R. Reddy, D. Mayerich, L. Deng, Q. Yu, G. Feng, H. A. Calderon, F. C. Robles Hernandez, Z. M. Wang, J. Bao, *Chem. Mater.* **2020**, *32*, 5009–5015.
[20] C. M. M. Soe, C. C. Stoumpos, M. Kepenekian, B. Traoré, H. Tsai, W. Nie, B. Wang, C. Katan, R. Seshadri, A. D. Mohite, J. Even, T. J. Marks, M. G. Kanatzidis, *J. Am. Chem. Soc.* **2017**, *139*, 16297–16309.
[21] L. Mao, W. Ke, L. Pedesseau, Y. Wu, C. Katan, J. Even, M. R. Wasielewski, C. C. Stoumpos, M. G. Kanatzidis, *J. Am. Chem. Soc.* **2018**, *140*, 3775–3783.
[22] D. B. Mitzi, C. A. Feild, W. T. A. Harrison, A. M. Guloy, *Nature* **1994**, *369*, 467–469.
[23] L. Li, Z. Sun, P. Wang, W. Hu, S. Wang, C. Ji, M. Hong, J. Luo, *Angew. Chem.* **2017**, *129*, 12318–12322.
[24] D. H. Kim, J. B. Whitaker, Z. Li, M. F. van Hest, K. Zhu, *Joule* **2018**, *2*, 1437–1451.
[25] G. E. Eperon, M. T. Hörantner, H. J. Snaith, *Nat. Chem. Rev.* **2017**, *1*.
[26] A. Babayigit, A. Ethirajan, M. Muller, B. Conings, *Nat. Mater.* **2016**, *15*, 247–251.
[27] H. J. Snaith, *Nat. Mater.* **2018**, *17*, 372–376.
[28] E. Berger, M. Bagheri, S. Asgari, J. Zhou, M. Kokkonen, P. Talebi, J. Luo, A. F. Nogueira, T. Watson, S. G. Hashmi, *Sustain. Energy Fuels* **2022**, *6*, 2879–2900.
[29] F. Giustino, H. J. Snaith, *ACS Energy Lett.* **2016**, *1*, 1233–1240.
[30] A. Mattoni, A. Filippetti, M. I. Saba, P. Delugas, *J. Phys. Chem. C* **2015**, *119*, 17421–17428.
[31] M. A. Carignano, A. Kachmar, J. Hutter, *J. Phys. Chem. C* **2015**, *119*, 8991–8997.
[32] M. B. Fridriksson, S. Maheshwari, F. C. Grozema, *J. Phys. Chem. C* **2020**, *124*, 22096–22104.
[33] C. M. M. Soe, G. P. Nagabhushana, R. Shivaramaiah, H. Tsai, W. Nie, J.-C. Blancon, F. Melkonyan, D. H. Cao, B. Traoré, L. Pedesseau, M. Kepenekian, C. Katan, J. Even, T. J. Marks, A. Navrotsky, A. D. Mohite, C. C. Stoumpos, M. G. Kanatzidis, *Proc. Natl. Acad. Sci. USA* **2018**, *116*, 58–66.
[34] K. Leng, I. Abdelwahab, I. Verzhbitskiy, M. Telychko, L. Chu, W. Fu, X. Chi, N. Guo, Z. Chen, Z. Chen, C. Zhang, Q.-H. Xu, J. Lu, M. Chhowalla, G. Eda, K. P. Loh, *Nat. Mater.* **2018**, *17*, 908–914.
[35] C. R. C. Rêgo, J. Schaarschmidt, T. Schlöder, M. Penaloza-Amion, S. Bag, T. Neumann, T. Strunk, W. Wenzel, *Front. Mater.* **2022**, *9*.
[36] L. Mao, Y. Wu, C. C. Stoumpos, B. Traore, C. Katan, J. Even, M. R. Wasielewski, M. G. Kanatzidis, *J. Am. Chem. Soc.* **2017**, *139*, 11956–11963.
[37] J. A. Alonso, M. J. Martínez-Lope, M. T. Casais, M. T. Fernández-Díaz, *Inorg. Chem.* **2000**, *39*, 917–923.
[38] K. Robinson, G. V. Gibbs, P. H. Ribbe, *Science* **1971**, *172*, 567–570.
[39] P. Hohenberg, W. Kohn, *Phys. Rev.* **1964**, *136*, B864–B871.
[40] W. Kohn, L. J. Sham, *Phys. Rev.* **1965**, *140*, A1133–A1138.
[41] D. D. Koelling, B. N. Harmon, *J. Phys. C* **1977**, *10*, 3107–3114.
[42] J. P. Perdew, K. Burke, M. Ernzerhof, *Phys. Rev. Lett.* **1996**, *77*, 3865–3868.
[43] P. E. Blöchl, *Phys. Rev. B* **1994**, *50*, 17953–17979.
[44] P. E. Blöchl, C. J. Först, J. Schimpl, *Bull. Mater. Sci.* **2003**, *26*, 33–41.
[45] G. Kresse, J. Hafner, *Phys. Rev. B* **1993**, *48*, 13115–13118.
[46] G. Kresse, J. Furthmüller, *Phys. Rev. B* **1996**, *54*, 11169–11186.
[47] S. Grimme, *J. Comput. Chem.* **2006**, *27*, 1787–1799.
[48] S. Grimme, J. Antony, S. Ehrlich, H. Krieg, *J. Chem. Phys.* **2010**, *132*.
[49] L. G. Ferreira, M. Marques, L. K. Teles, *Phys. Rev. B* **2008**, *78*, 125116.
[50] L. G. Ferreira, M. Marques, L. K. Teles, *Phys. Rev. B* **2008**, *78*.
[51] J. C. Slater, K. H. Johnson, *Phys. Rev. B* **1972**, *5*, 844–853.
[52] D. Guedes-Sobrinho, I. Guilhon, M. Marques, L. K. Teles, *J. Phys. Chem. Lett.* **2019**, *10*, 4245–4251.
[53] L. Octavio de Araujo, F. P. Sabino, C. R. C. Rêgo, D. Guedes-Sobrinho, *J. Phys. Chem. Lett.* **2021**, *12*, 7245–7251.
[54] D. Guedes-Sobrinho, D. N. Silveira, L. Octavio de Araujo, J. F. Dalmedico, W. Wenzel, Y. Pramudya, M. J. Piotrowski, C. R. C. Rêgo, *Sci. Rep.* **2023**, *13*, 4446.
[55] C. C. Stoumpos, C. M. M. Soe, H. Tsai, W. Nie, J.-C. Blancon, D. H. Cao, F. Liu, B. Traoré, C. Katan, J. Even, A. D. Mohite, M. G. Kanatzidis, *Chem* **2017**, *2*, 427–440.
[56] C. R. C. Rêgo, KIT-Workflows/DFT-VASP: DFT-VASP **2021**.
[57] J. Schaarschmidt, J. Yuan, T. Strunk, I. Kondov, S. P. Huber, G. Pizzi, L. Kahle, F. T. Bölle, I. E. Castelli, T. Vegge, F. Hanke, T. Hickel, J. Neugebauer, C. R. C. Rêgo, W. Wenzel, *Adv. Energy Mater.* **2021**, *12*.
[58] D. Cortecchia, S. Neutzner, J. Yin, T. Salim, A. R. Srimath Kandada, A. Bruno, Y. M. Lam, J. Martí-Rujas, A. Petrozza, C. Soci, *APL Mater.* **2018**, *6*.
[59] X. Chang, D. Marongiu, V. Sarritzu, N. Sestu, Q. Wang, S. Lai, A. Mattoni, A. Filippetti, F. Congiu, A. G. Lehmann, F. Quochi, M. Saba, A. Mura, G. Bongiovanni, *Adv. Funct. Mater.* **2019**, *29*.
[60] A. Morteza Najarian, F. Dinic, H. Chen, R. Sabatini, C. Zheng, A. Lough, T. Maris, M. I. Saidaminov, F. P. García de Arquer, O. Voznyy, S. Hoogland, E. H. Sargent, *Nature* **2023**, *620*, 328–335.
[61] D. Wang, P. Liang, Y. Dong, H. Shu, Z. Liu, *J. Phys. Chem. Solids* **2020**, *144*, 109510.
[62] L. Ma, M.-G. Ju, J. Dai, X. C. Zeng, *Nanoscale* **2018**, *10*, 11314–11319.
[63] K. A. P. Sousa, F. d M Morawski, C. E. M. de Campos, R. L. T. Parreira, M. J. Piotrowski, G. R. Nagurniak, C. L. Jost, *Electrochim. Acta* **2022**, *408*, 139945.
[64] J. P. C. S. Felix, K. E. A. Batista, W. O. Morais, G. R. Nagurniak, R. P. Orenha, C. R. C. Rêgo, D. Guedes-Sobrinho, R. L. T. Parreira, M. M. Ferrer, M. J. Piotrowski, *J. Comput. Chem.* **2022**, *44*, 1040–1051.
[65] D. H. Cao, C. C. Stoumpos, T. Yokoyama, J. L. Logsdon, T.-B. Song, O. K. Farha, M. R. Wasielewski, J. T. Hupp, M. G. Kanatzidis, *ACS Energy Lett.* **2017**, *2*, 982–990.
[66] M.-C. Jung, S. R. Raga, Y. Qi, *RSC Adv.* **2016**, *6*, 2819–2825.
[67] G. Wu, R. Liang, Z. Zhang, M. Ge, G. Xing, G. Sun, *Small* **2021**, *17*.

Manuscript received: February 5, 2024
Revised manuscript received: April 11, 2024
Accepted manuscript online: May 14, 2024
Version of record online: June 28, 2024